PHYSICS OF FLUIDS **27**, 072101 (2015)

Wave drag on a submerged sphere

Adrien Benusiglio,[1,2,a)] Frédéric Chevy,[3] Élie Raphaël,[4] and Christophe Clanet[1,2]

[1]*LadHyX, UMR 7646, CNRS, École Polytechnique, 91120 Palaiseau, France*
[2]*PMMH, UMR 7636, CNRS, ESPCI, 10 rue Vauquelin, 75005 Paris, France*
[3]*Laboratoire Kastler Brossel, CNRS, UPMC, ENS, 24 rue Lhomond, 75231 Paris, France*
[4]*PCT, UMR 7083, CNRS, Gulliver, PSL Research University, ESPCI ParisTech, 10 rue Vauquelin, 75005 Paris, France*

(Received 7 November 2014; accepted 23 June 2015; published online 7 July 2015)

We measure the wave drag acting on fully submerged spheres as a function of their depth and velocity, with an apparatus that measures only the component of the drag due to the proximity of the free surface. We observe that close to the surface the wave drag is of the order of the hydrodynamic drag. In our range of study, the measured force is more than one order smaller than predictions based on linear response. In order to investigate this discrepancy, we measure the amplitude of the waves at the origin of the wave drag, comparing the measurement with a theoretical model. The model captures the measurements at "large depth" but the wave's amplitude saturates at "small depth," an effect that partially accounts for the difference between the predicted and measured wave drag. © *2015 AIP Publishing LLC.* [http://dx.doi.org/10.1063/1.4923454]

I. INTRODUCTION

Objects moving at the surface of the sea create propagating waves that carry away energy. This loss of energy results in a resistive force, the wave drag, an added surface force discussed for the first time in the celebrated work of Lord Kelvin.[1] The wave drag theory has direct applications in naval engineering, to estimate the total drag of ships.[2] In the case of marine animals, biologists use this concept to explain swimming strategies close to the surface, like the depth distribution of fishes in a river, which avoid proximity to the surface[3] and the depth dependence of the swimming performance of trouts[4] or even the leaping of dolphins, taking into account the energetic cost of the proximity of the surface.[5] For humans, the wave drag plays a crucial role in swimming, as shown by measurements on submerged mannequins.[6]

Following the application of atomic force microscopy in soft matter systems, recent studies have focused on the wave drag on small objects.[7,8] Special interest was dedicated to velocities close to the minimum speed of the capillary gravity waves ($c_{\min}$), since it was shown theoretically that a discontinuity of the force could exist.[9–11] Experiments were performed using partially immersed objects, for which the contact line plays an important role and makes it difficult to compare the experimental results with theory. A first quantitative test of Raphaël and de Gennes[7] was recently obtained using Leidenfrost droplets of liquid nitrogen floating at the surface of water for which the hysteresis of the contact line is negligible.[12]

Another way of exploring wave drag without having to consider the role of the contact line is to study its effect on a fully submerged object; at small depth, it deforms the surface and creates a wake that takes away momentum and energy. The problem was theoretically treated by Michell[13] and Havelock[14] for spheres and later for spheroids using the method of images.[15] More recently, a self-consistent scheme taking into account the influence of the sphere on wave propagation was used to address the case of an immersed cylinder.[16] Here, we experimentally study the wave drag

a)Electronic mail: adrienb@stanford.edu. Current address: Department of Bioengineering, Stanford University, Stanford, California 94305, USA.

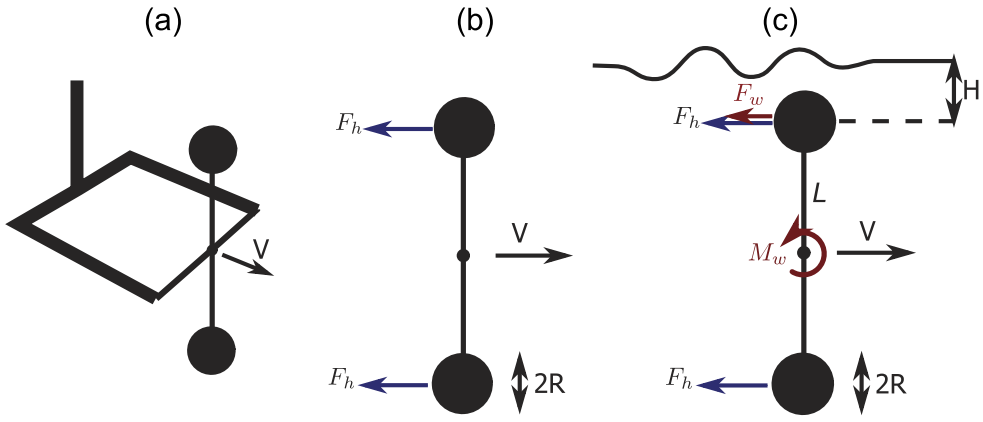

FIG. 1. Wave drag measurement apparatus: (a) apparatus plus external carrier arm. Side view: (b) far from the surface and (c) close to the surface.

and the wake-amplitude generated by fully submerged spheres as a function of their velocity and depth and compare measurements with existing theory.

II. WAVE DRAG MEASUREMENT APPARATUS

The experimental setup developed to measure the wave drag is presented in Fig. 1. It is composed of two smooth identical spheres connected by a 12 cm length and 1 mm diameter rod attached to a support by a torsion wire. The spheres are made of polyacetal (density 1.4×10^3 kg/m^3) and have a diameter $D = 2R = 1$, 2, or 3.76 cm accurate to the micron scale. The torsion wire is a nylon wire used for fishing, with a diameter ranging from 0.3 to 1 mm, depending on the magnitude of the force to be measured. The experiments are conducted in a towing tank of 3 m length, 60 cm width, and 60 cm depth filled with water (viscosity $\eta = 10^{-3}$ Pa s, surface tension $\gamma = 73 \times 10^{-3}$ N/m, density $\rho = 10^3$ kg/m^3, and optical index $n = 1.33$). The whole apparatus is towed with an external arm, through an underwater attachment 50 cm long, so that the wake of the carrier and the wake of the sphere do not interfere [Fig. 1(a)]. The apparatus is carried at a velocity V from 0 to 90 cm/s with the depth of the upper sphere H measured from the center of the sphere to the undisturbed surface, varying from one to several diameters (c). When the two spheres are far from the surface (b), they both are submitted to the same hydrodynamical drag F_h and we do not measure any torque. When the upper sphere gets closer to the surface (c), an added wave drag F_w is applied on the upper sphere and we measure a torque $M_w = F_w \times L$, which allows the measurement of the wave drag exerted on the upper sphere $F_w = M_w/L$, the hydrodynamic part of the drag being mechanically removed.

A preliminary test of the apparatus consists of measuring the hydrodynamic drag on one sphere, by removing the upper one (Fig. 2). In the experiments, the Reynolds number Re defined as $Re = \rho V R/\eta$ is in between roughly 500 and 4000 for the 1 cm sphere and 2000 and 16 000 for the 3.76 cm sphere, so that the hydrodynamic drag force is assumed to be purely inertial (proportional to V^2), as verified in Fig. 2(a) where we plot F_h as a function of V. We compare the drag coefficient $C_\mathrm{d} = F_\mathrm{h}/(\frac{1}{2}\rho V^2 \pi R^2)$ with experimental values from the literature[17] in Fig. 2(b), showing a reasonable agreement, and we observe in this figure that C_d is approximately constant in the range of study.

III. MEASUREMENTS

A. Dependence of the wave drag on the depth

Fig. 3 shows the wave drag of spheres of 1 and 2 cm diameter as a function of their depth, for several velocities. We observe that the wave drag increases with R/H and reaches a maximum when $R/H = 1$, i.e., when the sphere contacts the surface. The wave drag falls below the experimental

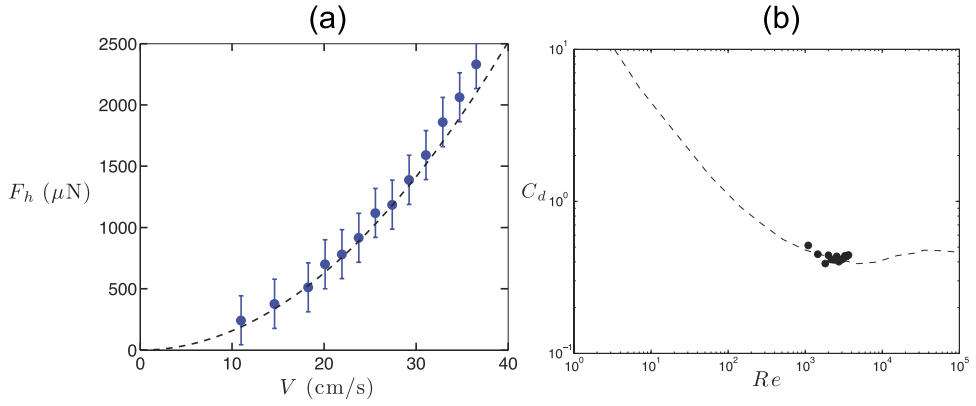

FIG. 2. (a) Hydrodynamical drag of a 2 cm diameter sphere. The dashed line is an estimation through the equation $F_h = \frac{1}{2}\rho V^2 \pi R^2 C_d$, with $C_d = 0.5$. The error bars represent the sensibility of the apparatus. (b) C_d as a function of Re; dots: measurements, dashed line: data from the literature.[17]

resolution when R/H is smaller than 0.3, i.e., when the top of the sphere is at a distance of one or more diameter away from the surface. Note that even for the largest sphere used in our study (D = 3.76 cm), the distance between the two connected spheres in the measurement apparatus is larger than 3 radii. In this regime, we can therefore neglect the hydrodynamical interaction between the two spheres. The horizontal dashed lines in Fig. 3 represent the hydrodynamic drag at large depth for the velocities considered, measured with the same apparatus, with only one sphere attached.

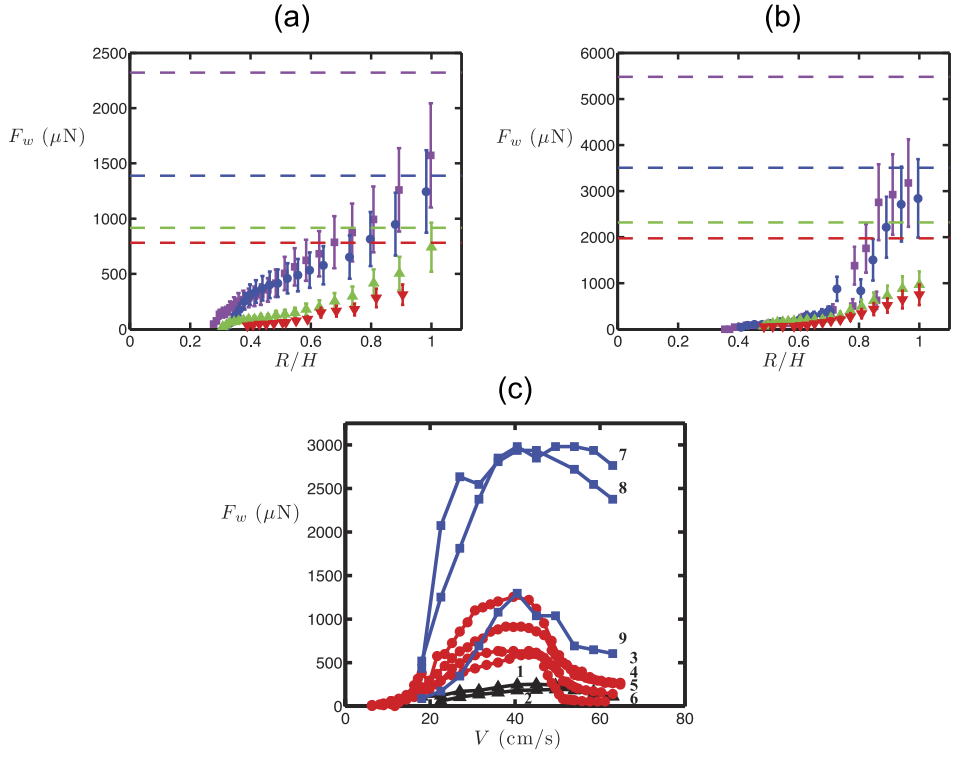

FIG. 3. Wave drag of immersed spheres as a function of R/H. (a) Sphere of 1 cm diameter and (b) sphere of 2 cm diameter. The symbols stand for various velocities: "■" 36.6 cm/s, "●" 29.2 cm/s, "▲" 23.8 cm/s, and "▼" 21.9 cm/s. The horizontal dashed lines represent the corresponding hydrodynamical drag for each velocity, the drag increasing with the velocity. (c) Wave drag as a function of the velocity for 3 sizes of spheres at different depths. The curve numbering refers to the experimental conditions given in Table I.

TABLE I. Experimental conditions for the data presented in Figs. 3(c) and 4. The two spheres are always connected by a 12 cm rod.

Sphere diameter (cm)	Curve n°	Depth (cm)	R/H
1	1	7.3	0.68
	2	8.1	0.62
2	3	12.3	0.81
	4	13.8	0.72
	5	17.4	0.57
	6	21.6	0.48
3.76	7	22.8	0.82
	8	24.3	0.77
	9	32.8	0.57

We observe that the maximum wave drag (when the sphere touches the surface) is of the order of the hydrodynamic drag, regardless the velocity, for the two sizes of spheres, and that it is larger than about half of the hydrodynamic drag when $R/H > 0.5$, that is, when the top of the sphere is at less than one radius from the free surface.

Fig. 3(c) shows the dependence of the wave drag on the velocity for three sizes of spheres at several depths for each sphere. We notice that the wave drag is not a monotonic function of the velocity, but increases, reaches a maximum, and decreases with the velocity. The velocity at which the maximum is reached slightly depends on the size of the spheres and their depth.

IV. MODEL AND DISCUSSION

In the low velocity and large depth limit where the wave drag can be calculated using the method of images, the force is given by[14]

$$F_w = \sqrt{\frac{2\pi^3 g^7}{H}}\rho R^6 V^{-5} \exp\left(-\frac{2gH}{V^2}\right). \quad (1)$$

We note that the derivation of Equation (1) requires two assumptions: First, in order to consider only one image, we need to have $R \ll H$, so that the velocity field created by the hydrodynamic image is negligible near the original sphere and does not affect the boundary conditions at its surface. Second, the application of Equation (1) requires that the propagation of the surface waves is not affected by the presence of the submerged sphere. Due to the harmonic nature of the potential flow describing the wave propagation, a disturbance of typical wavelength $\lambda = 2\pi/k$ will extend vertically over the same distance. Our approach thus requires that $kH \gg 1$.

In Fig. 4, we compare the measured wave drag and the theoretical prediction of Equation (1) as a function of the velocity, for two sizes of spheres. For every measurement, the experimental values are much smaller than the theoretical ones. Since the mirror image method is valid in the limit of deep objects, while we work in a regime $R \simeq H$, this discrepancy is most likely due to a saturation effect limiting the wake amplitude when the sphere is close to the surface. To confirm this interpretation, we now discuss the amplitude of the wave which can be measured for much deeper objects.

V. WAKE AMPLITUDE MEASUREMENTS

A. Optical apparatus

The experimental apparatus used to measure the amplitude of waves is illustrated in Figs. 5(a) and 5(b). The wake profile is optically measured on the path of the sphere ($y = 0$). The method is based on the refraction of light through surfaces: a vertical laser beam crosses the transparent

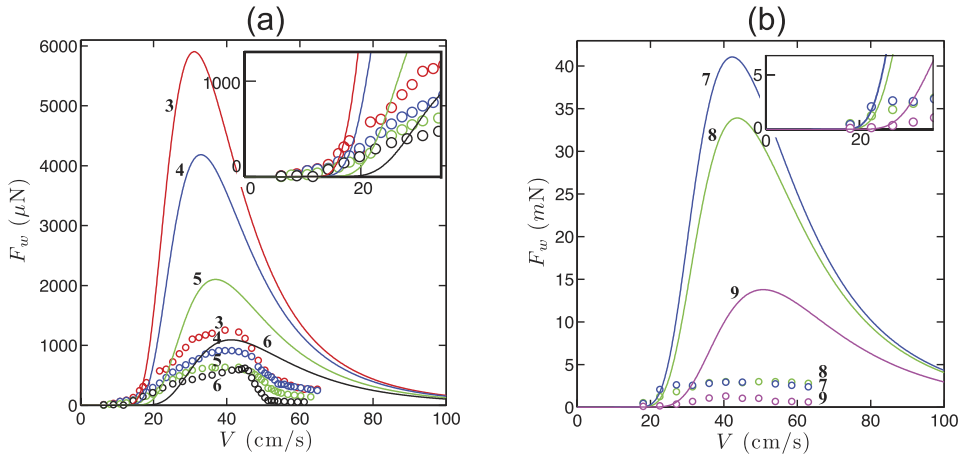

FIG. 4. Comparison of the measured wave drag and the theoretical prediction from Equation (1). (a) 2 cm sphere and (b) 3.76 cm sphere, theoretical predictions in solid line. The insets magnify the small velocities. The depth of measurement is indicated in Table I, the force decreasing with the depth.

bottom of the tank, is refracted through the free surface, and hits a horizontal screen above the water surface. From the deviation of the laser beam, we obtain the local slope of the surface that is integrated to estimate the surface profile. As the sphere crosses the laser beam, the integration gives a local measurement (for example, trough to crest) and not a global measurement. The experiments are conducted in the same towing tank. When the waves created by the spheres have a large slope (an amplitude larger than about 10% of the wavelength), they start breaking up, limiting the use of an optical method. In this limit, a capacitance wave height gauge is used for measurements (Akamina Technologies AWP-24).

B. Surface profilometry

In order to obtain a three dimensional measurement of the surface height and check the measurements obtained with the previous methods, we use a fringe projection profilometry method.[18,19] The method consists of projecting a fringe pattern on the water surface, with the water being saturated with white color particles. A Matlab program is used to compare images of the deformed and the un-deformed surface, estimate the phase shift of the fringes, and compute the surface profile. An example of pattern obtained above a submerged sphere moving from left to right is presented in Fig. 6(a). When not stated otherwise, the measurements are carried with any of the three methods.

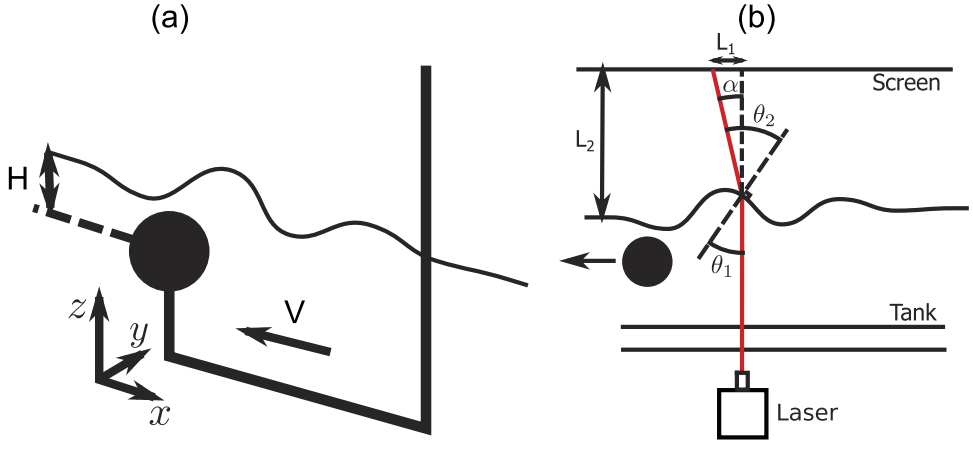

FIG. 5. Schematic of the wake measurement apparatus: (a) general view and (b) side view and conventions.

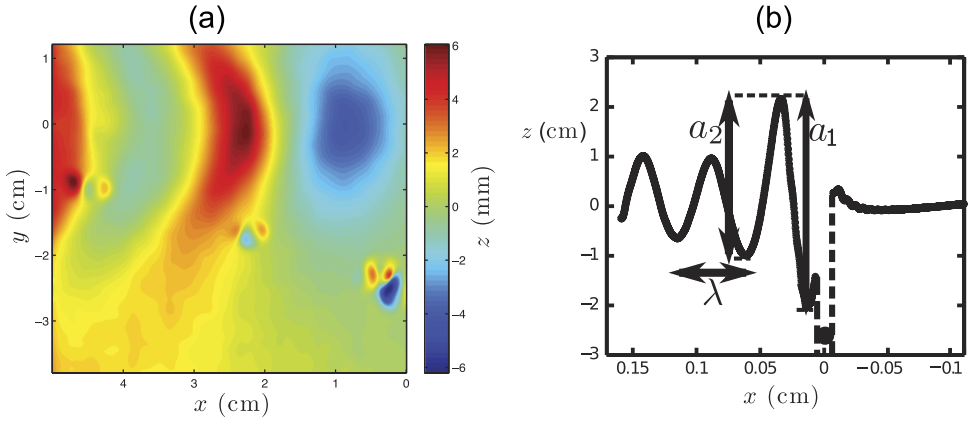

FIG. 6. (a) Surface height of the wake created by a submerged sphere of diameter $D = 3.76$ cm moving from left to right at $V = 45$ cm/s at a depth $H = 50$ mm, obtained by surface profilometry (Sec. V B). The color bar represents the surface height. (b) Wake profile above the 1 cm sphere path ($y = 0$) moving from left to right, with a_1, the amplitude of the first wave and a_2, the amplitude of the second wave, obtained with the optical apparatus (Sec. V A). The signal is lost when the sphere crosses the laser beam (vertical dashed lines). In (a) and (b), the sphere is at the position $x = 0$.

VI. MEASUREMENTS

Fig. 6(b) shows a typical measurement of the wake profile along the x axis by the optical apparatus, for a 1 cm sphere moving towards the negative x values. The gravity waves propagate behind the sphere ($x = [0 - 0.15]$ m), with an amplitude decreasing over several wavelengths. We define a_1 as the wake amplitude measured from the first trough to the first crest, and a_2, the amplitude measured from the first crest to the second trough.

Fig. 7 shows the amplitude a_1 as a function of H for 3 sizes of spheres, at three different velocities. For a given depth, the amplitude increases with the size of the sphere. At varying depths, the amplitude increases from the minimal sensitivity of our system at about three diameters deep, before saturating. Both the depth at which saturation is reached and the saturated value increase with the velocity.

VII. MODEL AND DISCUSSION

A. Scaling of the wave amplitude in the deep-object approximation

Using dimensional analysis, the displacement of the surface along x can be written as

$$\xi(x) = k_V^2 R^3 F(k_V R, k_V H, k_V x), \tag{2}$$

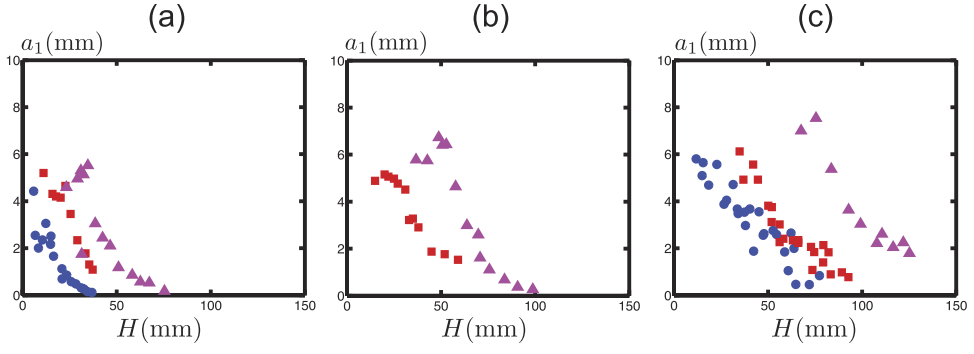

FIG. 7. Amplitude of the wake a_1 as a function of the depth, for three sizes of sphere. The symbols represent the sphere diameters, "•" 1 cm, "■" 2 cm, and "▲" 3.76 cm. The velocities are (a) $V = 29.2$ cm/s, (b) $V = 45$ cm/s, and (c) $V = 60$ cm/s.

with $k_V = g/V^2$ the typical wave-vector of the gravitational wake. In this expression, both viscosity and surface tension are absent, an approximation valid in the limit of large Reynolds numbers and of sphere larger than the capillary length.

In an infinite fluid, in the referential linked to the sphere, the flow is well represented by a superposition of a uniform flow of velocity $\boldsymbol{V}$ and a dipolar flow. A potential for this flow in polar coordinates takes the form $\Phi_{flow}(\boldsymbol{r} = (x, y, z)) = -\boldsymbol{V} \cdot \boldsymbol{r} - \frac{1}{2}\boldsymbol{V} \cdot \boldsymbol{r}\frac{R^3}{r^3}$, with the right term accounting for a dipolar flow. Here, we replace the sphere by a hydrodynamic dipole $\boldsymbol{P} = R^3\boldsymbol{V}$. In the linear approximation, we assume that the surface deformation is proportional to P, hence

$$\xi(x) = k_V^2 R^3 F(k_V H, k_V x). \tag{3}$$

In particular, we expect for the two amplitudes $a_{1,2}$ of Fig. 6(b)

$$\frac{a'_{i=1,2}}{R'^3} = f_i(H'), \tag{4}$$

with $a'_i = k_V a_i$, $R' = k_V R$, and $H' = k_V H$.

We verify the scaling for a_1 and a_2 in Fig. 8. To ensure that we are indeed in the deep-object approximation, we only consider data points such that $H/R \geq 2$ and $k_V H \geq 2$. We observe that for both a_1 and a_2, predicted scaling (4) is indeed satisfied.

B. Quantitative test of the mirror-dipole approximation

In the linear regime, we can calculate the surface deformation as done in Raphaël and de Gennes,[7] using the method of images to determine the expression of the pressure field acting on the surface. The deformation $\xi(x, y)$ of a liquid surface due to the external pressure field $p_0(x, y)$ moving at a constant velocity $\boldsymbol{V}$ is given by

$$\xi(x, y) = -\frac{1}{\rho}\int \frac{d^2\boldsymbol{k}}{(2\pi)^2}\left[\frac{e^{i\boldsymbol{k}\cdot\boldsymbol{r}_\perp}\widehat{p_0}(\boldsymbol{k})}{\omega_k^2 - (\boldsymbol{k}\cdot\boldsymbol{V})^2 - i\varepsilon \mathrm{sg}(\boldsymbol{k}\cdot\boldsymbol{V})}\right], \tag{5}$$

where $\boldsymbol{k}$ is the wave-vector in the plane (x, y), sg is the sign function, $\widehat{p_0}$ is the Fourier transform of p_0, $\boldsymbol{r}_\perp = (x, y)$, ρ is its magnitude, and ω_k is the dispersion relation of the surface waves; here $\omega_k = \sqrt{gk}$. The parameter ε describes the effect of a small viscosity and prevents the divergence of the integral. For low viscosity, we take the limit $\varepsilon \to 0^+$ in the final results.

In the present case, the perturbing pressure field p_0 is created by the presence of the immersed sphere of radius R. If the free surface is flat, the velocity field around the sphere can be obtained by the method of images, superposing the flow potential of the sphere and its successive images with respect to the surface. For a deep sphere ($H \gg R$), we can restrict ourselves to the first image of the

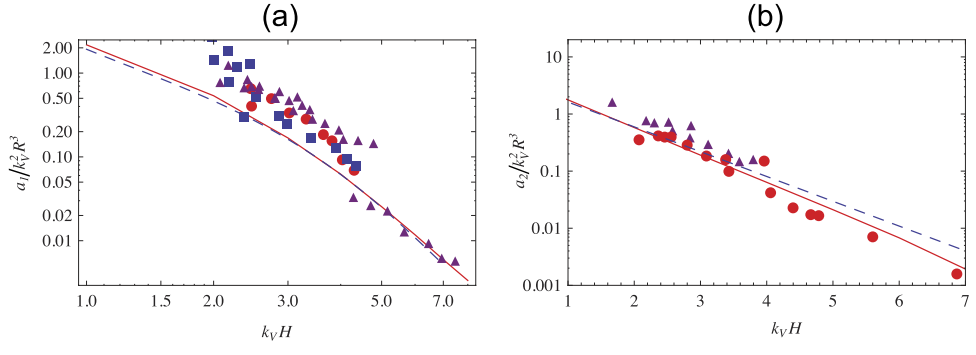

FIG. 8. Measurement of a_1 (a) and a_2 (b) vs depth. The symbols represent the sphere diameters, "•" 1 cm, "■" 2 cm, and "▲" 3.76 cm. The lines are the prediction of the mirror-dipole approximation. Solid line: numerical calculation of the integral [Equation (5)]. Dashed line: long range expansion, Equations (15) and (16). We keep here only the experimental points for which H is larger than $2R$.

dipole and we write for the total velocity potential $\Phi = \Phi_1 + \bar{\Phi}_1$, where

$$\Phi_1(\boldsymbol{r} = (x, y, z)) = -\frac{1}{2}\boldsymbol{V} \cdot \boldsymbol{r}\frac{R^3}{r^3} \tag{6}$$

is the velocity potential of a sphere moving at a velocity $\boldsymbol{V}$ and $\bar{\Phi}_1$ is the image of Φ_1 with respect to the free surface.

Let $P(x, y, z) = P_0 - \rho g z + p_0(x, y, z)$ the pressure field in the fluid, where P_0 is the atmospheric pressure and p_0 is the perturbation due to the sphere. Using Bernoulli's theorem, p_0 is given by

$$p_0 = \frac{\rho}{2}(V^2 - v(x, y, z)^2), \tag{7}$$

where $\boldsymbol{v} = \boldsymbol{V} + \boldsymbol{\nabla}\Phi$ is the total velocity field. Close to the free surface, the effect of the dipole is small compared to V, and we can expand this equation. We then obtain the pressure field at the free surface $p_0(x, y) \simeq 2\rho \boldsymbol{V}\boldsymbol{\nabla}\Phi_1$, where the factor 2 originates from the image dipole. A straightforward calculation shows that at the free surface, the Fourier transform of the pressure field exerted by the sphere is given by

$$\widehat{p_0}(\boldsymbol{k}) = 2\pi\rho R^3 \frac{(\boldsymbol{k} \cdot \boldsymbol{V})^2}{k} e^{-kH}. \tag{8}$$

Substituting this expression in Equation (5) yields

$$\xi(x, y) = -R^3 \int \frac{d^2\boldsymbol{k}}{2\pi} \left[\frac{(\boldsymbol{k} \cdot \boldsymbol{V})^2 e^{-kH}}{\omega_k^2 - (\boldsymbol{k} \cdot \boldsymbol{V})^2 + i\varepsilon \mathrm{sg}(\boldsymbol{k} \cdot \boldsymbol{V})} \right] e^{i\boldsymbol{k}\cdot\boldsymbol{r}_\perp}. \tag{9}$$

This equation can be recast as $\xi(x, y) = \xi_s(x, y) + \xi_a(x, y)$, where ξ_s (ξ_a) is the even (odd) component of the displacement and is formally given by

$$\xi_a(x, y) = \frac{iR^3}{2\pi} \int d^2\boldsymbol{k} (\boldsymbol{k} \cdot \boldsymbol{V})^2 e^{-kH} \mathrm{sg}(\boldsymbol{k} \cdot \boldsymbol{V}) \delta(\omega_k^2 - (\boldsymbol{k} \cdot \boldsymbol{V})^2) e^{i\boldsymbol{k}\cdot\boldsymbol{r}_\perp}, \tag{10}$$

$$\xi_s(x, y) = -R^3 \int \frac{d^2\boldsymbol{k}}{2\pi} \mathrm{PP} \left[\frac{(\boldsymbol{k} \cdot \boldsymbol{V})^2 e^{-kH}}{\omega_k^2 - (\boldsymbol{k} \cdot \boldsymbol{V})^2} \right] e^{i\boldsymbol{k}\cdot\boldsymbol{r}_\perp}, \tag{11}$$

where PP stands for the principal part.

These two components have different physical interpretations. As pointed out in Ref. 7, the wave drag is associated with the symmetry breaking of the surface deformation between the forward and backward directions and is therefore described by the anti-symmetric part ξ_a.

As observed experimentally, the gravitational waves propagate in the backward direction, which means that the forward component of the ξ_a must be canceled out by ξ_s. Conversely, the symmetric and antisymmetric components of the wake interfere constructively in the backward direction. As a consequence, the symmetric part is the sum of two components: a "bump" located above the immersed object and a propagative part.

The asymptotic expansion of ξ_a shows that far from the object, we have

$$\xi_a(x) = -\pi k_V^2 R^3 e^{-k_V H} J_0(k_V x), \tag{12}$$

where the Bessel function is typical of two-dimensional wave propagation. Since the antisymmetric part accounts for half the backward deformation, we expect the amplitude $\xi(x)$ of the backward gravitational wave to be given by

$$\xi(x) = -2\pi k_V^2 R^3 e^{-k_V H} J_0(k_V x). \tag{13}$$

Above the immersed sphere, the contribution of the antisymmetric part is by definition zero. We thus have $\xi(0) = \xi_s(0)$. In the limit $k_V H \to \infty$, the exponential term vanishes at $k = k_V$ and we obtain

$$\xi(0) \simeq -\frac{1}{k_V}\left(\frac{R^3}{H^3}\right). \tag{14}$$

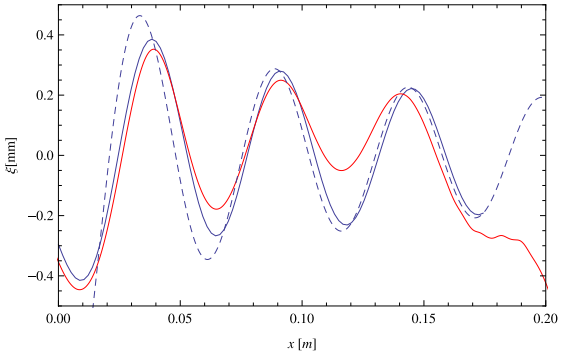

FIG. 9. Wake profile for a 2 cm sphere immersed at a depth $H = 3.7$ cm and moving at a velocity $V = 29.2$ cm/s. The red solid line corresponds to the experimental results (at $x > 17$ cm, the wake of the towing apparatus interferes). The blue solid line is the numerical calculation of $\xi(x)$ using the mirror dipole approximation and the blue dashed line is long range expansion (13). Here, the theoretical calculation is plotted without any adjustable parameter, except the choice of the axis origins.

Assuming that the first minimum is well described by Equation (14) while the first maximum is given by Equation (13), then we find for a_1,

$$a_1 \simeq k_V^2 R^3 \left[\frac{1}{k_V^3 H^3} + 0.4 \times 2\pi e^{-k_V H} \right], \tag{15}$$

where the coefficient 0.4 corresponds to the value of the first minimum of J_0.

Similarly, using the distance between the first minimum and the second maximum for J_0, one gets the approximate expression

$$a_2 \simeq 0.7 \times 2\pi k_V^2 R^3 e^{-k_V H}. \tag{16}$$

In Fig. 8, we compare the predictions with the measurements and we observe a good agreement between experiment and theory in the deep-object approximation $k_V H, H/R \gg 1$ with an increasing discrepancy as the depth decreases.

We observe in Fig. 9 that both the analytic and numerical predictions for $\xi(x)$ agree rather well with the experimental data without any adjustable parameter for a very deep sphere. The only small difference between the curves is the existence of a stronger decay of the wake in experiments, which can be accounted for by introducing viscosity in the model.

C. Maximum amplitude

The dipolar approximation is governed by two small parameters. First, we consider only one image of the original sphere to express the velocity potential. This approximation does not take into account the boundary condition at the surface of the sphere and is therefore valid only if the two sphere are far enough, i.e., if $R/H \ll 1$. Second, we also assumed that, in the derivation of the wave drag and of the surface deformation, the propagation of the surface waves was not affected by the presence of the submersed sphere. Since a surface wave creates a disturbance over a depth $\simeq k_V^{-1}$, this approximation is valid only for $H \ll 1/k_V$. These two constraints are represented graphically in Fig. 10(a) where we observe readily that the breakdown of the dipolar approximation will be caused by the first process for $k_V R \gtrsim 1$.

These deviations to the dipolar predictions are observed experimentally when we plot a_1 on a larger range of values of H. In this case, we observe that the wake amplitude saturates as the depth decreases (Fig. 7). We define $a^*(V) = \max_H[a_1(H,V)]$. On a dimensional ground, a^* must scale as $a^* = Rf(1/k_V R)$. To confirm this simple scaling, in Fig. 10, we plot a^*/R versus $1/k_V R$ for several values of R. We observe that the data points collapse on a single curve. In this figure, we can identify two regimes. On the one hand, a^*/R is constant for $k_V R \ll 1$, and we therefore have $a^* \propto R$. On the other hand, we observe that for $k_V R \gg 1$, $a^*/R \propto 1/k_V R$; hence $a^* \propto V^2/g = \lambda_V$.

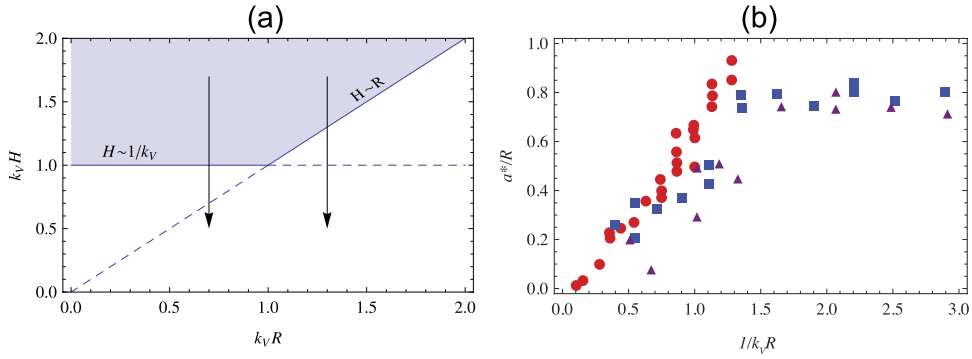

FIG. 10. (a) The mirror-dipole approximation is valid in the gray area (note that the sphere surfaces for $H = R$). When we measure ξ vs H at fixed sphere radius and velocity, we move along a vertical line in the $(k_V R, k_V H)$ plane. As pictured by the two arrows, depending on the value of $k_V R$, the saturation of the amplitude occurs for $H \simeq R$ ($H \simeq k_V^{-1}$) if $R \gg k_V^{-1}$ ($R \ll k_V^{-1}$). (b) Experimental measurement of the maximum amplitude a^*. Red disks: $D = 9.4$ cm; blue squares: $D = 3.76$ cm; and purple triangles: $D = 2$ cm.

We can recover the low-velocity behavior by noting that for $R \simeq H$ and $k_V R \gg 1$, Equation (15) becomes $a_1 \simeq \lambda_V$, which yields the correct scaling.

D. Deviation from linearity

In our range of measurement of the wave drag, the wave amplitude is always saturated and not well depicted by the model. One way to account for the importance of the saturation of the waves is to rescale the theoretical wave drag by $(a^*/a_1)^2$ with a^* the measured saturated value of the wave amplitude and a_1 the theoretical prediction from the model, the energy carried by a wave being dependent of its square amplitude.[20] a^* is measured at the velocity $V = 29$ cm/s for the 2 cm spheres and at $V = 45$ cm/s for the largest spheres, around the velocity of maximum wave drag, and the theoretical wake amplitude a_1 is estimated at the same velocities from Equation (15). We observe in Fig. 11 that once rescaled, we recover a better order of magnitude for the predicted wave drag. This *ad hoc* correction of the theoretical prediction is very crude and does not completely capture the measurements as it is done by rescaling the force measuring the amplitude of the waves in only one direction of propagation, when the waves' amplitude depends on their direction of propagation. Therefore, a more complete comparison of the wave pattern could be a start to improve the prediction even further.

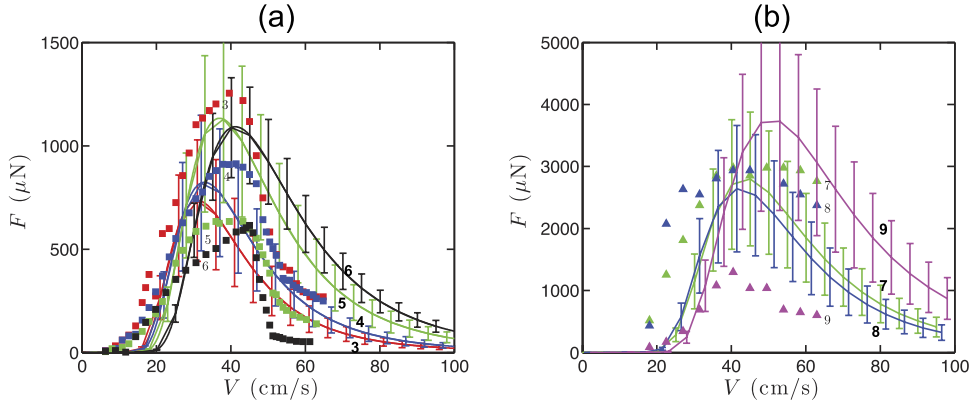

FIG. 11. Comparison of the measured wave drag (symbols) and the theoretical prediction (lines) as a function of the velocity for 2 cm spheres (a) and 3.76 cm spheres (b). The depths of measurement (numbering in regular for measurements and bold for prediction) are indicated in Table I. The theoretical curves are rescaled by a factor $(a^*/a_1)^2$, estimated at 29.24 cm/s (a) and 45 cm/s (b), and error bars are based on the error in this rescaling.

VIII. CONCLUSION

We measure the wave drag of submerged spheres. The wave drag is of the same order as the hydrodynamic drag when the top of the sphere is at less than one sphere radius from the surface. It confirms the importance of the wave drag for objects navigating close to the surface, marine animals, and swimmers. In this range, the wave drag estimated with the method of images is a lot larger than the measurements. We measure the wake amplitude and observe that it is well captured by an estimation by the method of images at "large depth" but saturates to a maximal value at "small depth." Taking into account the saturation of the wake amplitude on the path of the sphere it is possible to partially correct the wave drag estimation and obtain the right order of magnitude of the force. A more precise correction may be obtained by measuring the amplitude of all the components of the wake rather than only the waves propagation opposite to the direction of propagation.

ACKNOWLEDGMENTS

We wish to thank D. Quéré for helpful discussions and M. Le Merrer for her help with the experimental setup. The study was funded with both a Ph.D. grant (A.B.) and a financial support from the French "Direction Générale de l'Armement" (DGA).

[1] W. Thomson, "On the waves produced by a single impulse in water of any depth, or in a dispersive medium," Proc. R. Soc. London **42**, 80–83 (1887).
[2] R. B. Chapman, "Hydrodynamic drag of semisubmerged ships," J. Basic Eng. **94**, 879 (1972).
[3] N. F. Hughes, "The wave-drag hypothesis: An explanation for size-based lateral segregation during the upstream migration of salmonids," Can. J. Fish. Aquat. Sci. **61**, 103–109 (2004).
[4] P. W. Webb, D. Sims, and W. W. Schultz, "The effects of an air/water surface on the fast-start performance of rainbow trout (oncorhynchus mykiss)," J. Exp. Biol. **155**, 219–226 (1991).
[5] D. Weihs, "Dynamics of dolphin porpoising revisited," Integr. Comp. Biol. **42**, 1071–1078 (2002).
[6] R. Vennell, D. Pease, and B. Wilson, "Wave drag on human swimmers," J. Biomech. **39**, 664–671 (2006).
[7] É. Raphaël and P.-G. de Gennes, "Capillary gravity waves caused by a moving disturbance: Wave resistance," Phys. Rev. E **53**, 3448 (1996).
[8] D. Richard and E. Raphael, "Capillary-gravity waves: The effect of viscosity on the wave resistance," EPL **48**, 49 (1999).
[9] T. Burghelea and V. Steinberg, "Onset of wave drag due to generation of capillary–gravity waves by a moving object as a critical phenomenon," Phys. Rev. Lett. **86**, 2557–2560 (2001).
[10] J. Browaeys, J.-C. Bacri, R. Perzynski, and M. Shliomis, "Capillary-gravity wave resistance in ordinary and magnetic fluids," Europhys. Lett. **53**, 209 (2001).
[11] F. Chevy and É. Raphaël, "Capillary gravity waves: A fixed-depth analysis," EPL **61**, 796 (2003).
[12] M. Le Merrer, C. Clanet, D. Quéré, É. Raphaël, and F. Chevy, "Wave drag on floating bodies," Proc. Natl. Acad. Sci. U. S. A. **108**, 15064–15068 (2011).
[13] J. H. Michell, "The wave-resistance of a ship," Philos. Mag. **45**, 106 (1898).
[14] T. H. Havelock, "Some cases of wave motion due to a submerged obstacle," Proc. R. Soc. A **93**, 520–532 (1917).
[15] T. H. Havelock, "The wave resistance of a spheroid," Proc. R. Soc. A **131**, 275–285 (1931).
[16] A. Chepelianskii, M. Schindler, F. Chevy, and E. Raphaël, "Self-consistent theory of capillary–gravity-wave generation by small moving objects," Phys. Rev. E **81**, 016306 (2010).
[17] R. L. C. Flemmer and C. L. Banks, "On the drag coefficient of a sphere," Powder Technol. **48**, 217–221 (1986).
[18] A. Maurel, P. Cobelli, V. Pagneux, and P. Petitjeans, "Experimental and theoretical inspection of the phase-to-height relation in Fourier transform profilometry," Appl. Opt. **48**, 380–392 (2009).
[19] P. J. Cobelli, A. Maurel, V. Pagneux, and P. Petitjeans, "Global measurement of water waves by Fourier transform profilometry," Exp. Fluids **46**, 1037–1047 (2009).
[20] J. Lighthill, *Waves in Fluids* (Cambridge University Press, 1978).